nanomaterials

MDPI

Article

Atomic Insights into Ti Doping on the Stability Enhancement of Truncated Octahedron $LiMn_2O_4$ Nanoparticles

Wangqiong Xu [1], Hongkai Li [1], Yonghui Zheng [1], Weibin Lei [1], Zhenguo Wang [1], Yan Cheng [1], Ruijuan Qi [1,*], Hui Peng [1], Hechun Lin [1], Fangyu Yue [1] and Rong Huang [1,2,*]

[1] Key Laboratory of Polar Materials and Devices (MOE) and Department of Electronics, East China Normal University, Shanghai 200062, China; wangqiongx@126.com (W.X.); hongkaizzz@foxmail.com (H.L.); yhzheng@phy.ecnu.edu.cn (Y.Z.); weibinleilove@126.com (W.L.); wzgcoinmail@126.com (Z.W.); ycheng@ee.ecnu.edu.cn (Y.C.); hpeng@ee.ecnu.edu.cn (H.P.); hclin@ee.ecnu.edu.cn (H.L.); fyyue@ee.ecnu.edu.cn (F.Y.)

[2] Collaborative Innovation Center of Extreme Optics, Shanxi University, Taiyuan 030006, Shanxi, China

* Correspondence: rjqi@ee.ecnu.edu.cn (R.Q.); rhuang@ee.ecnu.edu.cn (R.H.)

Abstract: Ti-doped truncated octahedron $LiTi_xMn_{2-x}O_4$ nanocomposites were synthesized through a facile hydrothermal treatment and calcination process. By using spherical aberration-corrected scanning transmission electron microscopy (Cs-STEM), the effects of Ti-doping on the structure evolution and stability enhancement of $LiMn_2O_4$ are revealed. It is found that truncated octahedrons are easily formed in Ti doping $LiMn_2O_4$ material. Structural characterizations reveal that most of the Ti^{4+} ions are composed into the spinel to form a more stable spinel $LiTi_xMn_{2-x}O_4$ phase framework in bulk. However, a portion of Ti^{4+} ions occupy 8a sites around the {001} plane surface to form a new $TiMn_2O_4$-like structure. The combination of $LiTi_xMn_{2-x}O_4$ frameworks in bulk and the $TiMn_2O_4$-like structure at the surface may enhance the stability of the spinel $LiMn_2O_4$. Our findings demonstrate the critical role of Ti doping in the surface chemical and structural evolution of $LiMn_2O_4$ and may guide the design principle for viable electrode materials.

Keywords: truncated octahedral $LiMn_2O_4$; Ti doping; crystal planes; cathode materials; Li-ion batteries

Citation: Xu, W.; Li, H.; Zheng, Y.; Lei, W.; Wang, Z.; Cheng, Y.; Qi, R.; Peng, H.; Lin, H.; Yue, F.; et al. Atomic Insights into Ti Doping on the Stability Enhancement of Truncated Octahedron $LiMn_2O_4$ Nanoparticles. *Nanomaterials* **2021**, *11*, 508. https://doi.org/10.3390/nano11020508

Academic Editor: Jong-Min Lim

Received: 19 January 2021
Accepted: 15 February 2021
Published: 17 February 2021

1. Introduction

Rechargeable lithium-ion batteries (LIBs) have been regarded as promising energy storage and conversion devices for wearable mobile devices, electric vehicles (EVs), hybrid electric vehicles (HEVs), and stationary energy storage wells [1–3]. Among the various lithium-ion battery cathode materials, spinel $LiMn_2O_4$ is believed to hold huge potential for fulfilling the field-use requirements because of its good thermal stability, low cost, environmental friendliness, and three-dimensional channel structure [4–6]. Nevertheless, the practical applications of $LiMn_2O_4$ cathodes are restricted by the capacity fading during charge–discharge cycles, especially at elevated temperatures ($\geq$ 55 °C), which can be ascribed to the Mn dissolution and Jahn–Teller distortion [7,8].

In order to tackle these challenges, efforts have been paid to stabilize the structure of $LiMn_2O_4$. By doping with monovalent (e.g., Li^+ [9]), divalent (e.g., Mg^{2+} [10] and Ni^{2+} [11]) or trivalent (e.g., Al^{3+} [12], Co^{3+} [13] and Fe^{3+} [14]) metal ions, the average manganese ion valence is slightly increased, and therefore the Jahn–Teller effect is suppressed and a promoted cycling performance is obtained in the 4 V region. However, when $LiMn_2O_4$ works in the 2.0–4.8 V, inactive Mn^{4+} ions in the 4 V regions are further reduced to Mn^{3+} ions, and the cycle performance of low-valent ions doped materials is not that satisfactory. For example, Lee et al. [15] found that the $LiAl_{0.1}Mn_{1.9}O_4$ achieved capacity retention of 70% after 50 cycles in the 2.0–4.3 V range. When cycled between 2.0 and 5.0 V, the $LiNi_{0.5}Mn_{1.5}O_4$ shows a capacity retention value of about 65% [16]. Since the bond energy of Ti-O (662 kJ mol^{-1}) is higher than that of Mn-O (402 kJ mol^{-1}), the Mn^{4+} in

the lattice of $LiMn_2O_4$ could be partly replaced by Ti^{4+} to form a more stable spinel framework, i.e., $[Mn_{2-x}Ti_x]O_4$, therefore enhancing the stability of the spinel $LiMn_2O_4$. Recently, He et al. [17] reported that 72% capacity retention was achieved with the $LiTi_{0.5}Mn_{1.5}O_4$ electrode after 150 cycles performed between 2.0 and 4.8 V. By using an in situ X-ray diffraction technique, Wang et al. [18] found that Ti^{4+} ions can also suppress the Jahn–Teller distortion and stabilize the spinel structure during the charging/discharging process. Moreover, Ti substitution improves the structural stability of spinel cathode material as reported at large [19–21]. Although these findings are important and intriguing, a deep understanding on how Ti doping contributes to the stability enhancement of $LiMn_2O_4$ is still lacking.

To date, various experimental and computational results show that the structural stability of $LiMn_2O_4$ is strongly related to its surface structure [22–25]. Karim et al. [26] ascribed the improved stability of $LiMn_2O_4$ to the creation of a partial inverse spinel arrangement in the (111) surface. A further example by Ouyang et al. [27] showed that covering the $LiMn_2O_4$ (001) surface with Al_2O_3 changed the oxidation state of surface Mn atoms from +3 to +4, which is beneficial for the improvement in $LiMn_2O_4$ stability. Nevertheless, few studies have been undertaken to reveal the surface structure and chemical evolution of Ti-doped $LiMn_2O_4$ at atomic levels.

In this work, Ti-doped truncated octahedron $LiMn_2O_4$ samples are synthesized through a facile hydrothermal treatment and calcination process. To reveal the underlying mechanism of Ti-doping on the structure evolution and stability enhancement of $LiMn_2O_4$, morphology and phase characterization are performed by powder X-ray diffraction (XRD), scanning electron microscope (SEM), and Raman spectroscopy. X-ray photoelectron spectroscopy (XPS) further reveals that Ti ions are in a tetravalent oxidation state; after Ti ion doping, the percentage of Mn^{4+} in $LiTi_{0.5}Mn_{1.5}O_4$ reduced, suggesting the successful replacement of Mn^{4+} by Ti^{4+}. The surface evolution of $LiTi_xMn_{2-x}O_4$ (001) planes was investigated using the spherical aberration-corrected scanning transmission electron microscopes (Cs-STEM) technique. It is found that there is a more stable spinel $LiTi_xMn_{2-x}O_4$ formed in bulk, as well as at the {111} and {110} planes. In addition, for the first time, a $TiMn_2O_4$-like structure formed at {001} surface is observed by the Cs-STEM technique, which can reduce the surface energy of {001} planes and accelerate the growth rate of {001} planes. In addition, the $TiMn_2O_4$-like structure at {001} surface might improve the stability of $LiMn_2O_4$. According to the electron energy-loss spectroscopy (EELS) analysis, the appearance of the $TiMn_2O_4$-like phase is associated with the enrichment of Ti^{4+}. This work provides a comprehensive understanding of the influence of Ti doping on the evolutions of morphology, surface structure, and electronic structure of $LiMn_2O_4$ cathodes, which will benefit the further optimization of the electrochemical performance.

2. Materials and Methods

2.1. Sample Preparation

The $LiTi_xMn_{2-x}O_4$ ($0 \leq x \leq 0.5$) samples were synthesized by hydrothermal treatment and a calcination process [28,29], as depicted in Figure 1. First, to get Mn_3O_4 nanoparticles with better reaction activity and smaller particle size, commercially purchased Mn_3O_4 powders (1.0 g) were dispersed into NaOH aqueous solution (30 mL, 5 mol dm^{-3}) and magnetically stirred for 1 h. Afterward, the dispersion was transferred to a Teflon-lined stainless-steel autoclave (50 mL) and heated at 205 °C for 4 d in an oven. The final precipitated products were washed repeatedly with deionized water. The obtained Mn_3O_4 precursor was subsequently dried at 70 °C for 12 h in air. Then, the as-prepared Mn_3O_4 precursor, $LiNO_3$, $LiCl{\cdot}H_2O$, and TiO_2 (rutile) were ground in a mortar for 30 min and burned in the air at 500 °C for 3 h. The obtained Ti-doped $LiMn_2O_4$ precursors were washed repeatedly in deionized water to remove chlorion and nitrate impurities. Finally, the obtained Ti-doped $LiMn_2O_4$ precursor was calcined in air at 700 °C for 6 h. The final products were obtained after cooling to room temperature.

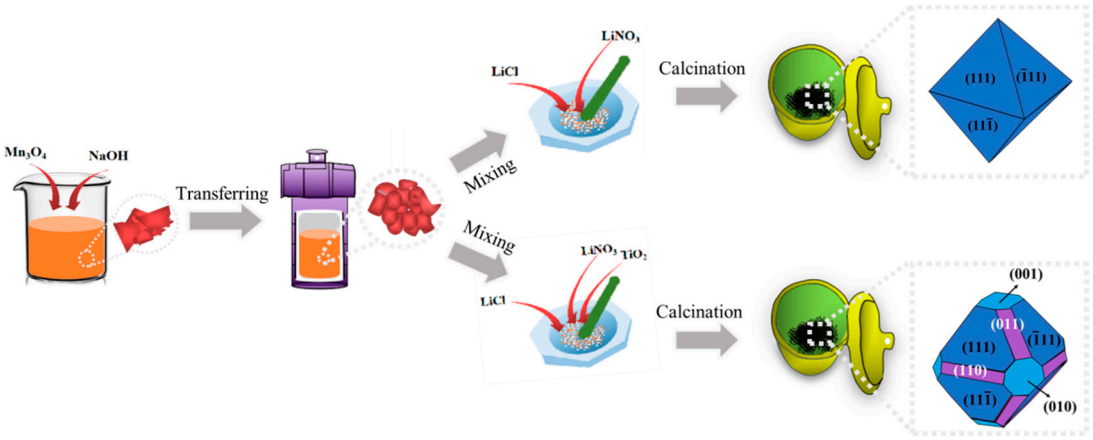

Figure 1. Schematic diagram of the preparation process of the $LiTi_xMn_{2-x}O_4$ samples.

2.2. Sample Characterization

The crystal structures were characterized by X-ray diffraction (XRD, D8, Bruker, Germany) with Cu Kα radiation; the data were collected between 10 and 80 degrees at an increment of 0.02 degrees. The size and morphology of the samples were observed by scanning electron microscope (SEM, S-4800, Hitachi, Japan). The crystal quality and defects were characterized by Raman spectra using a micro-Raman spectrometer (Jobin Yvon LabRAM HR 800UV, Longjumeau, France) with a 532 nm laser source. EDS mapping was performed with an Oxford Inca EDS detector on the JEOL 2100F, operated in the dark field scanning transmission electron microscopy (STEM, JEOL) mode. X-ray photoelectron spectroscopy (XPS, Thermo Fischer, ESCALAB 250Xi, Walham, MA, USA) measurements were performed to investigate the valence states of the materials, using the value of 284.8 eV as the C 1s peak reference. High-angle annular dark-field scanning transmission electron microscopy (HAADF-STEM) imaging and electron energy-loss spectroscopy (EELS) were performed with a spherical aberration-corrected (Cs-corrected) scanning transmission electron microscopy (STEM) operated at 300 kV (JEM-ARM300F, JEOL).

3. Results and Discussions

The phase and crystal structure of the samples are examined by XRD, as shown in Figure 2a. The diffraction peaks of all samples can be indexed to the standard pattern of spinel $LiMn_2O_4$ (JCPDS card No.35-0782; space group Fd-3m (No. 227)) without any impurity phases. More importantly, the relative peak intensities reflect the dominant surface orientations of each sample. Compared to the octahedron, the peaks on the (400), (440), and (311) lattice planes (Figure S1a–c) are more obvious in truncated octahedron samples after normalizing peaks to the dominant (111) octahedral orientation. With the increase in Ti content, the diffraction peaks shift toward lower angles, suggesting the increase in lattice parameters. The detailed lattice parameters of the $LiTi_xMn_{2-x}O_4$ (x = 0, 0.1, 0.2, 0.3, 0.4, 0.5) samples were calculated and are listed in Table S1. Since the atom radius of Ti^{4+} (0.061 Å) is larger than that of Mn^{4+} (0.053 Å) [30], the enlargement of the lattice constant indicates the substitution of Mn^{4+} by Ti^{4+} in the lattice, in line with previous reports [31].

Furthermore, the microstructure vibration of $LiTi_xMn_{2-x}O_4$ with different Ti doping content (Figure 2b) is investigated by Raman spectroscopy. The medium peak at about 480 cm^{-1} has $F_{2g}^{(2)}$ symmetry, while the weak bands observed at 400 and 370 cm^{-1} have the E_g and $F_{2g}^{(3)}$ symmetry, respectively [32,33]. The weak peak at 370 cm^{-1} is related to the Li-O symmetric vibration, i.e., connecting to the tetrahedral cation movements ($F_{2g}^{(3)}$) [34]. A very weak band at 285 cm^{-1} might be associated with the translation mode of lattice vibration [35]. A strong Raman peak at ~640 (±5) cm^{-1} could be assigned the symmetric Mn–O stretching vibration of [MnO_6] octahedron (A_{1g} mode). Moreover, a blue shift below x = 0.2 and a redshift above x = 0.2 are observed (Figure S1d), which further confirms the substitution of Ti atoms.

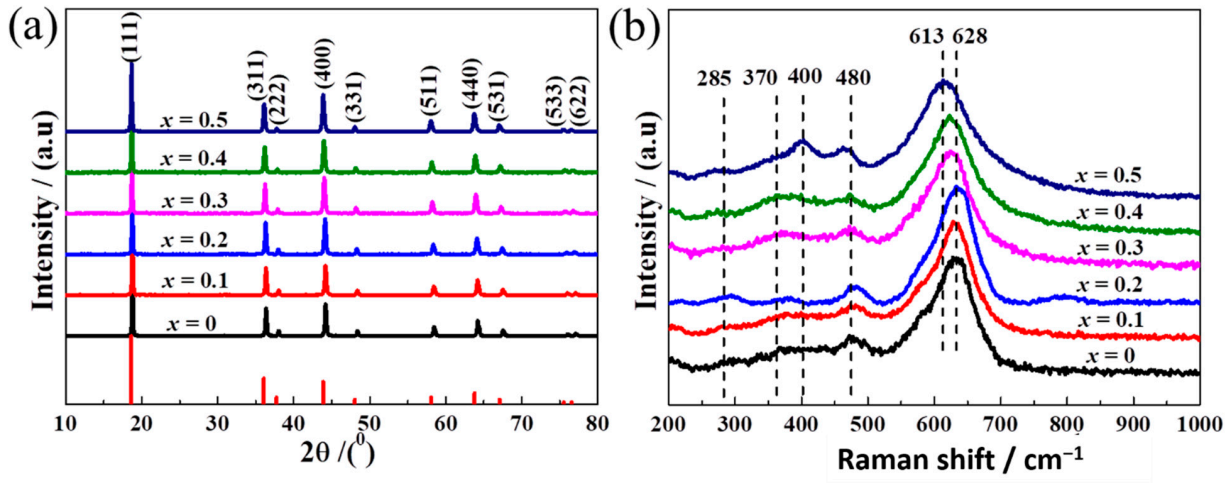

Figure 2. XRD patterns **(a)** and Raman spectra **(b)** of the $LiTi_xMn_{2-x}O_4$ (x = 0, 0.1, 0.2, 0.3, 0.4, 0.5) samples.

As shown in Figure 3a-f, the surface morphology and particle size of $LiTi_xMn_{2-x}O_4$ (x = 0, 0.1, 0.2, 0.3, 0.4, 0.5) were studied by SEM. The pristine $LiMn_2O_4$ (Figure 3a) is the prototype octahedral shape, which is bounded by eight {111} planes. It is reported that the truncated octahedral structure is beneficial for improving the high-rate capability and prolonging the cycle stability of LIBs, as the {111} planes can mitigate Mn dissolution while the truncated {110} and {001} planes facilitate Li^+ diffusion [8]. Though several strategies have been proposed to obtain truncated octahedral structures [5,36–38], in this report we find that Ti doping is beneficial to synthesize a truncated octahedral shape. With the increase in Ti concentration, the growth rate is increased in the (001) plane (red rectangle), reduced in the (111) plane (blue lines), and remains the same in the (110) plane (green lines), implying that the Ti doping can reduce the surface energy of the (001) planes. In addition, the particle size is also increased with the doping of the Ti element (Figure S2), which may result from the substitution of Ti with Mn element.

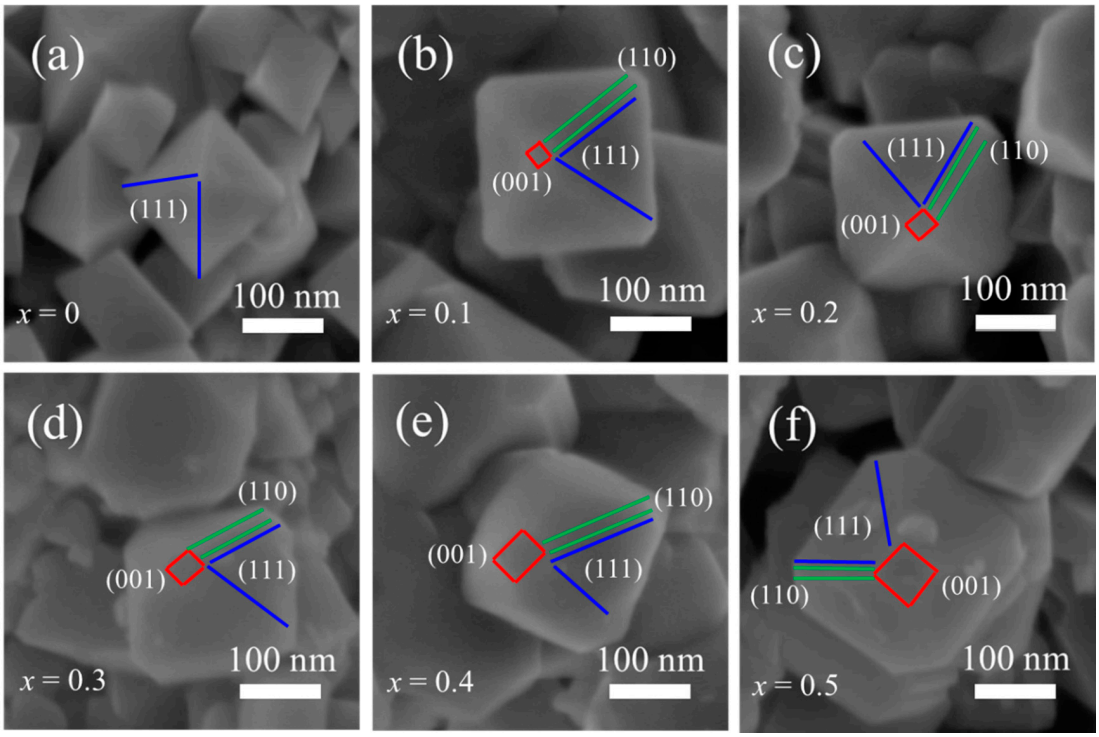

Figure 3. SEM images of $LiTi_xMn_{2-x}O_4$ at different concentrations (x = 0, 0.1, 0.2, 0.3, 0.4, 0.5) (**a–f**).

To further examine the valence states of elements in the mixed-valence compounds, XPS was performed for $LiMn_2O_4$ and $LiTi_{0.5}Mn_{1.5}O_4$, respectively. Figure 4a shows that the peaks of Ti $2p_{3/2}$ and Ti $2p_{1/2}$ in $LiTi_{0.5}Mn_{1.5}O_4$ are located at 458.2 and 463.8 eV, respectively, with 5.6 eV spin-orbit components, indicating that the Ti ions are in the tetravalent oxidation state [31,39]. As for the Mn 2p XPS spectra, two main peaks corresponding to the spin-orbit splitting of Mn $2p_{3/2}$ and Mn $2p_{1/2}$ are observed in $LiMn_2O_4$ and $LiTi_{0.5}Mn_{1.5}O_4$ (Figure 4b) [40]. Since the full width at half-maximum (FWHM) of the Mn $2p_{3/2}$ peaks are both larger than 3.5 eV, the oxidation states of Mn are expected to be between +3 and +4 valence. Furthermore, curve-fitting was conducted on the Mn $2p_{3/2}$ spectra (Figure 4c,d, see the fitting parameters in the supporting information in Tables S2 and S3) to evaluate the percentage of Mn^{3+} and Mn^{4+} ions [41,42]. The results show that the concentration of Mn^{4+} reduces from 47.28% to 42.13%, while the concentration of Mn^{3+} increases from 52.72% to 57.86% due to the substitution of Ti^{4+} ions (x = 0.5), as observed in Figure 4a.

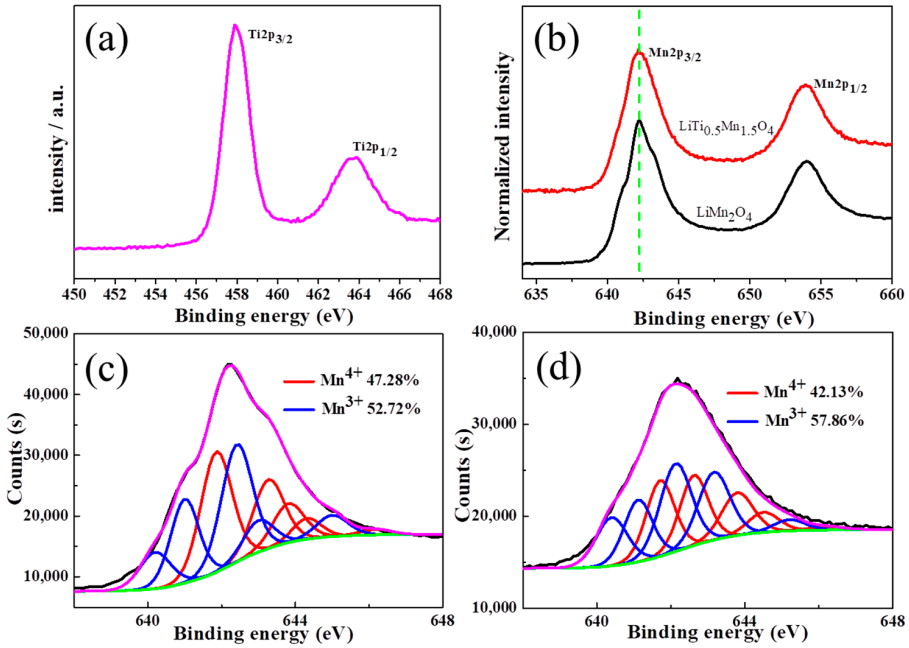

Figure 4. Ti 2p XPS spectra of $LiTi_{0.5}Mn_{1.5}O_4$ (**a**). Mn 2p XPS spectra (**b**) of $LiMn_2O_4$ and $LiTi_{0.5}Mn_{1.5}O_4$. Fitted spectra of $LiMn_2O_4$ (**c**) and $LiTi_{0.5}Mn_{1.5}O_4$ (**d**).

To reveal the underlying mechanism of Ti-doping on the structure evolution and stability enhancement of $LiMn_2O_4$, samples with different Ti doping concentrations were systematically investigated using the Cs-STEM technique [43]. Figure 5a verifies the octahedron characteristic of $LiMn_2O_4$ composed of {111} facets, and Figure 5b is the enlarged HAADF image, taken along the [110] direction around the (111) surface. Since the contrast of the HAADF-STEM image is roughly proportional to the square of the atomic number Z [44], the Li (Z = 3) and O (Z = 8) are invisible, while the Mn (Z = 25) could be detected. The Mn diamond configuration was clearly observed (Figure 5b), in line with the previously reported [45], showing a homogeneous microstructure from the bulk to the surface.

As for the $LiTi_{0.5}Mn_{1.5}O_4$, truncated octahedrons composed of {111} facets, {110} and {001} facets were observed. A uniform distribution of the Mn, O, and Ti elements is also shown in Figure S3. Similar to Figure 5b, the spinel crystal structure in $LiTi_{0.5}Mn_{1.5}O_4$ is also stable from the bulk to the surface in (111) planes according to the HAADF image (Figure 5d) taken along [110] orientation. This homogenous situation also happened in the (110) plane, as depicted in Figure 5e. However, a phase transition from the bulk to the surface appears progressively in (001) planes, as indicated by the cyan line. Though the atomic configuration in the bulk region (red rectangle) is similar to Figure 5d–e, the surface region (purple rectangle) is quite different. The contrast of the atoms at Li tetrahedral sites

becomes brighter and visible, which can be attributed to the substitution of heavy Ti or Mn (TM) ions [46]. This is also further confirmed by the line profiles shown in Figure 5i, in which the spacing in the surface area (d = 8.69 Å) is larger than the bulk area (d = 8.20 Å).

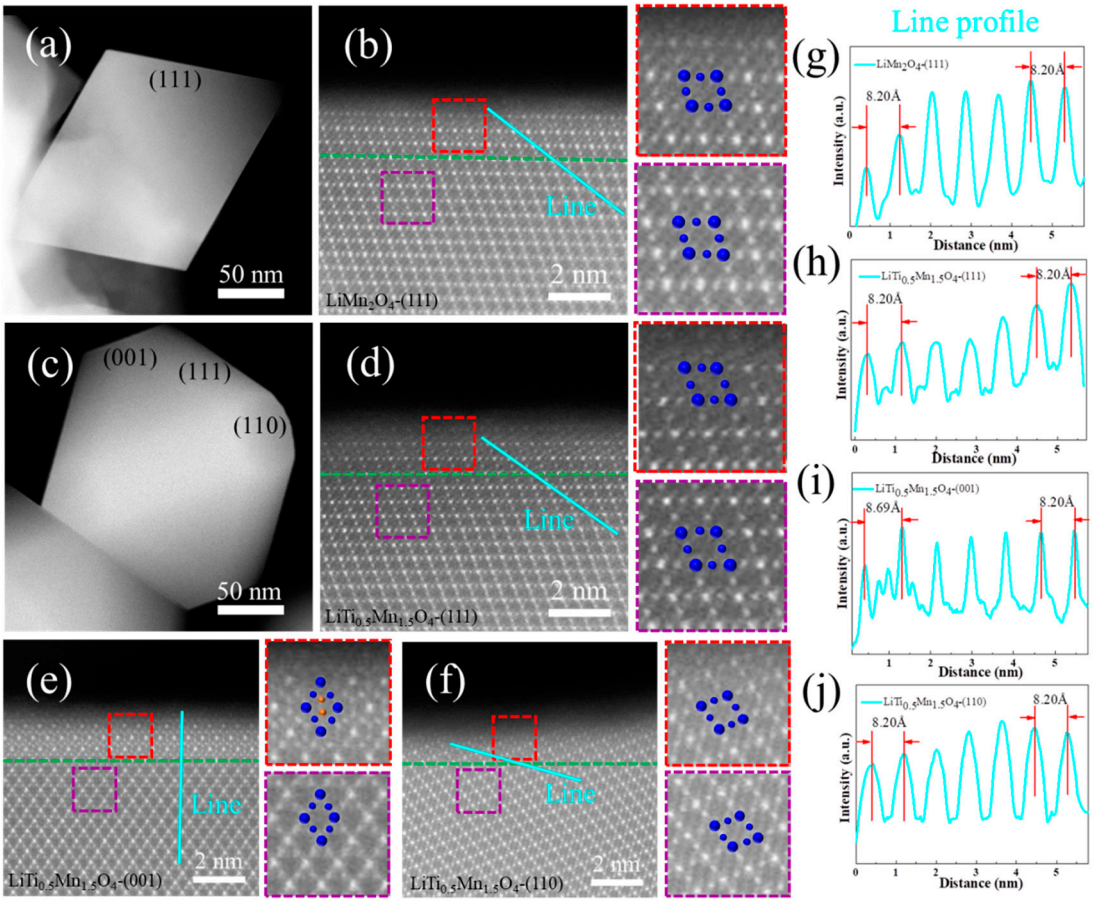

Figure 5. Low-magnification (a) and high-resolution (b) high-angle annular dark-field (HAADF) images of the $LiMn_2O_4$ viewed from the [110] crystallographic direction in (111) planes. Low-magnification (c) and high-resolution HAADF images of the $LiTi_{0.5}Mn_{1.5}O_4$ particles viewed from the [110] crystallographic direction in the (111) plane (d), (001) plane (e), and (110) plane (f). Magnified views of selected regions are shown in the right panels, where the contrast corresponding to the Mn columns at 16d and 8a sites are indicated by blue and orange spheres, respectively. The boundary between the bulk and the surface regions is marked by the green dashed line. Line profiles (g–j) correspond to the sky blue lines in panel (b,d–f), respectively.

We inspected the crystal structure of $LiMn_2O_4$, $TiMn_2O_4$, and Mn_3O_4 along the [110] direction, as shown in Figure 6a–c. Though the atomic arrangement is similar, the long diagonals (n) for $TiMn_2O_4$ (n = 8.679 Å) is significantly higher than that of $LiMn_2O_4$ (n = 8.245 Å) and Mn_3O_4 (n = 8.15 Å). Thus, the new phase formed at (001) surface is expected to be $TiMn_2O_4$, which can help to combat the impedance growth [47] and promote the electrochemical performance of high-voltage spinel $LiNi_{0.5}Mn_{1.5}O_4$. In short, the majority of the Ti atoms could replace Mn element in the bulk area and form a stable $LiTi_xMn_{2-x}O_4$ framework, which complies well with the XRD results. In addition, there is a new phase similar to $TiMn_2O_4$ formed at the spinel $LiMn_2O_4$ (001) surface.

It is known that the surface energy is gradually reduced in the sequence of {001}, {110} and {111} [48], thus the presence of the $TiMn_2O_4$-like spinel phase on the (001) surface may be related to the surface energy difference. Thus, the {001} plane is in accordance with the most unstable surfaces, favoring the Ti cations shift. Moreover, the Li-terminated $LiMn_2O_4$ {001} surfaces are also very unstable due to the increased dangling bonds and lower bonding energy with the oxygen anions [49]. Therefore, a small amount of TM

cations can exchange the position with Li^+, resulting in the formation of reconstruction layers in these regions. This reconstruction layers ($TiMn_2O_4$-like) are able to produce a more stable cathode/electrolyte interfacial layer due to the stronger Ti-O bond, promoting the stability of cathode materials [21].

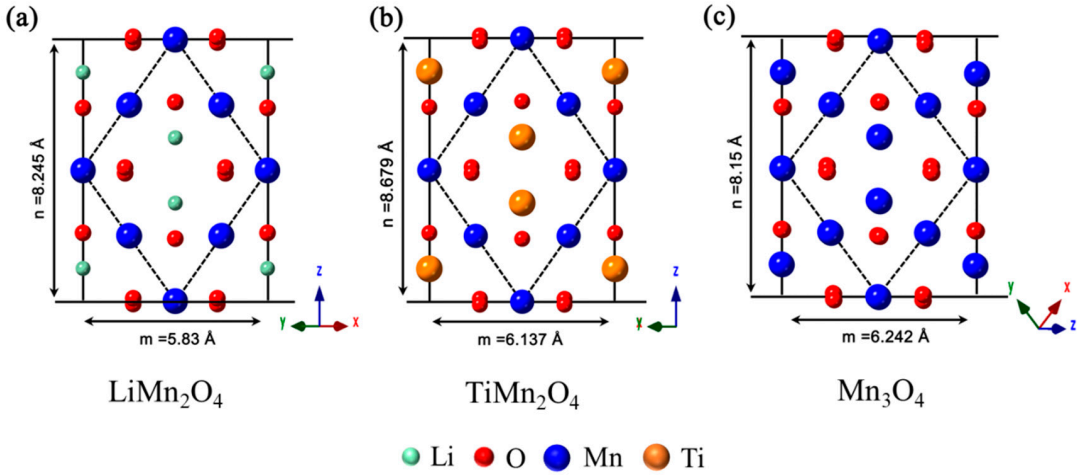

Figure 6. Crystal structure of the $LiMn_2O_4$ (a), $TiMn_2O_4$ (b), and Mn_3O_4 (c) viewed along the [110] direction.

To further unveil the change in surface chemical states around different crystal planes, the pristine $LiMn_2O_4$ and $LiTi_{0.5}Mn_{1.5}O_4$ samples are characterized using EELS, and the results are shown in Figure 7a–c. Figure 7a shows the Ti-$L_{2,3}$, O-K, and Mn-$L_{2,3}$ energy-loss near-edge fine structure (ELNES) around the (111) facet surface for the $LiMn_2O_4$, and the (111), (110), and (001) facet surfaces for the $LiTi_{0.5}Mn_{1.5}O_4$ after background subtraction and normalization. In $LiTi_{0.5}Mn_{1.5}O_4$, the pre-peak intensity of the O-K edge in $LiTi_{0.5}Mn_{1.5}O_4$ is slightly less than that in $LiMn_2O_4$, which is correlated with a slight decrease in Mn valence [50]. Moreover, the O-K spectrum in $LiMn_2O_4$ shows a sharp peak followed by a shoulder structure, while two peaks at 532.4 and 534.2 eV in $LiTi_{0.5}Mn_{1.5}O_4$ are observed, which can be assigned to the transition to the 3d bands of tetravalent Ti. Four peaks in the Ti-$L_{2,3}$ ELNES for $LiTi_{0.5}Mn_{1.5}O_4$ at different facets are also shown in Figure 7a, a fingerprint of Ti^{4+}, which is also consistent with the XPS measurement. By using the pristine $LiMn_2O_4$ as a reference to extract the k-factors (Figure S4), the Mn/O ratios ($R_{Mn/O}$) at different surface planes were quantified (Figure 7b), in which $R_{Mn/O}(110) > R_{Mn/O}(111) > R_{Mn/O}(001)$ planes. In the (001) plane, $R_{Mn/O}(001)$ is approximately 0.39, indicating that Ti^{4+} is enriched in the (001) plane. Furthermore, the relationship between the Mn (L_3/L_2) intensity ratio and the Mn valence state at different facets is investigated (Figure 7c). A higher L_3/L_2 value results in a decreased Mn valence state [51–54], originating from the Ti doping effect as claimed in Figure 7a.

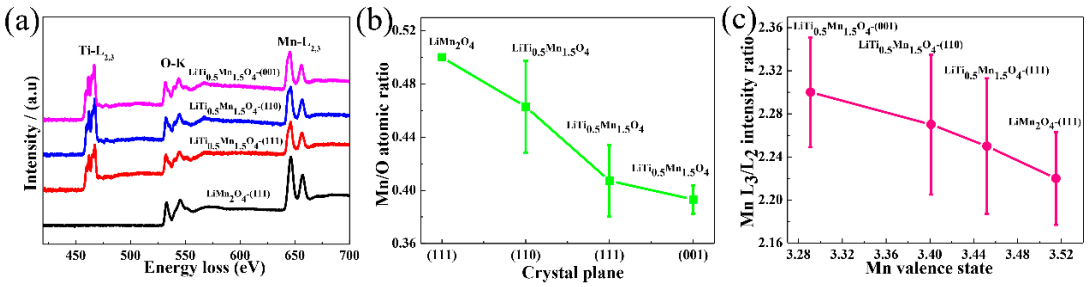

Figure 7. ELNES spectra of Ti-$L_{2,3}$, O-K, and Mn-$L_{2,3}$ from the surface of the (111) facet of the $LiMn_2O_4$, and (111), (110), and (001) facets of the $LiTi_{0.5}Mn_{1.5}O_4$ (**a**). Mn/O atomic ratio of $LiTi_{0.5}Mn_{1.5}O_5$ (**b**). Pristine $LiMn_2O_4$ was used as a reference to extract the k factors. Dependence of the Mn (L_3/L_2) intensity ratio vs. the Mn valence state in the (111) facet of the $LiMn_2O_4$, and (111), (110), and (001) facets of the $LiTi_{0.5}Mn_{1.5}O_4$ (**c**).

4. Conclusions

In conclusion, Ti-doped truncated octahedron $LiMn_2O_4$ samples were synthesized by a facile hydrothermal treatment and calcination process. Cs-STEM and chemical analysis techniques were carried out to reveal the underlying mechanism of Ti doping on the structure evolution and the stability enhancement of $LiMn_2O_4$ samples with different contents of Ti doping. It is found that Ti doping is beneficial to forming truncated octahedron $LiTi_xMn_{2-x}O_4$. Among the samples, $LiTi_{0.5}Mn_{1.5}O_4$ samples exhibit the most obvious truncated octahedron structure. After Ti ion doping, the percentage of Mn^{4+} in $LiTi_{0.5}Mn_{1.5}O_4$ reduced, suggesting the successful replacement of Mn^{4+} with Ti^{4+}. Based on detailed surface structural analysis of the {111}, {110}, and {001} planes of $LiTi_{0.5}Mn_{1.5}O_4$ at the atomic scale, it is found that there is a more stable spinel $LiTi_xMn_{2-x}O_4$ framework formed in bulk, as well as at the (111) and (110) planes. In addition, a $TiMn_2O_4$-like structure at the {001} surface is observed and thoroughly analyzed by Cs-STEM combined with EELS techniques. The new $TiMn_2O_4$-like structure can reduce the surface energy of (100) planes and accelerate the growth rate of (100) planes, therefore enhancing the stability of the spinel $LiMn_2O_4$. According to the EELS analysis, the appearance of the $TiMn_2O_4$-like phase can be associated with the enrichment of Ti^{4+}. Our findings demonstrate the critical role of the Ti ion doping in the surface chemical and structural evolution of $LiMn_2O_4$, which provides a facile method for high-stability cathode materials design and growth.

Supplementary Materials: The following are available online at https://www.mdpi.com/2079-4991/11/2/508/s1, Figure S1: Enlarged view of XRD patterns (a–c) at (311), (400) and (440), and microscopic view of raman spectra at 620 cm^{-1} (d), Figure S2: SEM images of the $LiTi_xMn_{2-x}O_4$ (x = 0, 0.1, 0.2, 0.3, 0.4, 0.5) at low magnification, and their corresponding to particle size distribution, Figure S3: STEM image and EDS elemental mappings of the $LiTi_{0.5}Mn_{1.5}O_4$ samples, Figure S4: Details to quantification the ratio of Mn and O, Table S1: Lattice parameters of $LiTi_xMn_{2-x}O_4$ (x = 0, 0.1, 0.2, 0.3, 0.4, 0.5), Table S2: Mn $2p_{3/2}$ peak parameters for Mn in $LiMn_2O_4$ sample, Table S3: Mn $2p_{3/2}$ peak parameters for Mn in $LiTi_{0.5}Mn_{1.5}O_4$ sample.

Author Contributions: W.X., R.Q. and R.H. conceived and designed the research and wrote the manuscript. W.X. carried out all of the experiments. Y.Z., Y.C., and F.Y. helped with the analysis of the STEM results. H.L. (Hongkai Li), W.L., and Z.W. were involved in the XPS experiments. H.P. and H.L. (Hechun Lin) were involved in the material syntheses. All authors have read and agreed to the published version of the manuscript.

Funding: This work was supported by the National Key Research and Development Program of China (2017YFA0303403), Shanghai Science and Technology Innovation Action Plan (No.19JC1416700), and the National Natural Science Foundation of China (Grant No. 61974042 and 11774092).

Data Availability Statement: The data presented in this study are openly available in [repository name e.g., FigShare] at [**doi**], reference number [reference number].

Conflicts of Interest: The authors declare no conflict of interest.

References

1. House, R.A.; Bruce, P.G. Lightning Fast Conduction. *Nat. Energy* **2020**, *5*, 191–192. [CrossRef]
2. Yu, X.; Deng, J.; Yang, X.; Li, J.; Huang, Z.-H.; Li, B.; Kang, F. A Dual-Carbon-Anchoring Strategy to Fabricate Flexible $LiMn_2O_4$ Cathode for Advanced Lithium-Ion Batteries with High Areal Capacity. *Nano Energy* **2020**, *67*, 104256. [CrossRef]
3. Shin, M.; Song, W.-J.; Han, J.-G.; Hwang, C.; Lee, S.; Yoo, S.; Park, S.; Song, H.-K.; Yoo, S.; Choi, N.-S.; et al. Metamorphosis of Seaweeds into Multitalented Materials for Energy Storage Applications. *Adv. Energy Mater.* **2019**, *9*, 1900570. [CrossRef]
4. Jeong, M.; Lee, M.-J.; Cho, J.; Lee, S. Surface Mn Oxidation State Controlled Spinel $LiMn_2O_4$ as a Cathode Material for High-Energy Li-Ion Batteries. *Adv. Energy Mater.* **2015**, *5*, 1500440. [CrossRef]
5. Jiang, C.; Tang, Z.; Wang, S.; Zhang, Z. A Truncated Octahedral Spinel $LiMn_2O_4$ as High-Performance Cathode Material for Ultrafast and Long-Life Lithium-Ion Batteries. *J. Power Sources* **2017**, *357*, 144–148. [CrossRef]
6. Lee, S.; Yoon, G.; Jeong, M.; Lee, M.-J.; Kang, K.; Cho, J. Hierarchical Surface Atomic Structure of a Manganese-Based Spinel Cathode for Lithium-Ion Batteries. *J. Power Sources* **2015**, *54*, 1153–1158.
7. Cai, Z.; Ma, Y.; Huang, X.; Yan, X.; Yu, Z.; Zhang, S.; Song, G.; Xu, Y.; Wen, C.; Yang, W. High Electrochemical Stability Al-Doped Spinel $LiMn_2O_4$ Cathode Material for Li-Ion Batteries. *J. Energy Storage* **2020**, *27*, 101036. [CrossRef]

8. Hou, Y.; Chang, K.; Tang, H.; Li, B.; Hou, Y.; Chang, Z. Drastic Enhancement in the Rate and Cyclic Behavior of $LiMn_2O_4$ Electrodes at Elevated Temperatures by Phosphorus Doping. *Electrochim. Acta* **2019**, *319*, 587–595. [CrossRef]
9. Gao, Y.; Dahn, J.R. Synthesis and Characterization of $Li_{1+X}Mn_{2-X}O_4$ for Li-Ion Battery Applications. *J. Electrochem. Soc.* **1996**, *143*, 100–114. [CrossRef]
10. Huang, J.; Yang, F.; Guo, Y.; Peng, C.; Bai, H.; Peng, J.; Guo, J. $LiMg_XMn_2$-XO_4 ($X \leq 0.10$) Cathode Materials with High Rate Performance Prepared by Molten-Salt Combustion at Low Temperature. *Ceram. Int.* **2015**, *41*, 9662–9667. [CrossRef]
11. Zhang, W.; Sun, X.; Tang, Y.; Xia, H.; Zeng, Y.; Qiao, L.; Zhu, Z.; Lv, Z.; Zhang, Y.; Ge, X.; et al. Lowering Charge Transfer Barrier of $LiMn_2O_4$ Via Nickel Surface Doping to Enhance Li^+ Intercalation Kinetics at Subzero Temperatures. *J. Am. Chem. Soc.* **2019**, *141*, 14038–14042. [CrossRef] [PubMed]
12. Zhan, D.; Liang, Y.; Cui, P.; Xiao, Z. Al-Doped $LiMn_2O_4$ Single Crystalline Nanorods with Enhanced Elevated-Temperature Electrochemical Performance Via a Template-Engaged Method as a Cathode Material for Lithium Ion Batteries. *Rsc Adv.* **2015**, *5*, 6372–6377. [CrossRef]
13. Kim, K.J.; Lee, J.H.; Koh, T.Y.; Kim, M.H. Improved Cyclic Stability by Octahedral Co^{3+} Substitution in Spinel Lithium Manganese Oxide Thin-Film Cathode for Rechargeable Microbattery. *Electrochim. Acta* **2016**, *200*, 84–89. [CrossRef]
14. Liu, H.; Tian, R.; Jiang, Y.; Tan, X.; Chen, J.; Zhang, L.; Guo, Y.; Wang, H.; Sun, L.; Chu, W. On the Drastically Improved Performance of Fe-Doped $LiMn_2O_4$ Nanoparticles Prepared by a Facile Solution-Gelation Route. *Electrochim. Acta* **2015**, *180*, 138–146. [CrossRef]
15. Lee, Y.S.; Lee, H.J.; Yoshio, M. New Findings: Structural Changes in $LiAl_XMn_{2-X}O_4$. *Electrochem. Commun.* **2001**, *3*, 20–23. [CrossRef]
16. Lee, E.-S.; Nam, K.-W.; Hu, E.; Manthiram, A. Influence of Cation Ordering and Lattice Distortion on the Charge-Discharge Behavior of $LiMn_{1.5}Ni_{0.5}O_4$ Spinel between 5.0 and 2.0 V. *Chem. Mater.* **2012**, *24*, 3610–3620. [CrossRef]
17. He, G.; Li, Y.; Li, J.; Yang, Y. Spinel $LiMn_{2-X}Ti_XO_4$ (X=0.5, 0.8) with High Capacity and Enhanced Cycling Stability Synthesized by a Modified Sol-Gel Method. *Solid-State Lett.* **2010**, *13*, A19–A21. [CrossRef]
18. Wang, S.; Yang, J.; Wu, X.; Li, Y.; Gong, Z.; Wen, W.; Lin, M.; Yang, J.; Yang, Y. Toward High Capacity and Stable Manganese-Spinel Electrode Materials: A Case Study of Ti-Substituted System. *J. Power Sources* **2014**, *245*, 570–578. [CrossRef]
19. Chen, R.; Knapp, M.; Yavuz, M.; Heinzmann, R.; Wang, D.; Ren, S.; Trouillet, V.; Lebedkin, S.; Doyle, S.; Hahn, H.; et al. Reversible Li^+ Storage in a $LiMnTiO_4$ Spinel and Its Structural Transition Mechanisms. *J. Phys. Chem. C* **2014**, *118*, 12608–12616. [CrossRef]
20. Lin, M.; Wang, S.H.; Gong, Z.L.; Huang, X.K.; Yang, Y. A Strategy to Improve Cyclic Performance of $LiNi_{0.5}Mn_{1.5}O_4$ in a Wide Voltage Region by Ti-Doping. *J. Electrochem. Soc.* **2013**, *160*, A3036–A3040. [CrossRef]
21. Kim, J.-H.; Pieczonka, N.P.W.; Lu, P.; Liu, Z.; Qiao, R.; Yang, W.; Tessema, M.M.; Sun, Y.-K.; Powell, B.R. In Situ Formation of a Cathode-Electrolyte Interface with Enhanced Stability by Titanium Substitution for High Voltage Spinel Lithium-Ion Batteries. *Adv. Mater. Interfaces* **2015**, *2*, 1500109. [CrossRef]
22. Benedek, R.; Thackeray, M.M. Simulation of the Surface Structure of Lithium Manganese Oxide Spinel. *Phys. Rev. B* **2011**, *83*, 195439. [CrossRef]
23. Kim, S.; Aykol, M.; Wolverton, C. Surface Phase Diagram and Stability of (001) and (111) $LiMn_2O_4$ Spinel Oxides. *Phys. Rev. B* **2015**, *92*, 115411. [CrossRef]
24. Warburton, R.E.; Iddir, H.; Curtiss, L.A.; Greeley, J. Thermodynamic Stability of Low- and High-Index Spinel $LiMn_2O_4$ Surface Terminations. *ACS Appl. Mater. Interfaces* **2016**, *8*, 11108–11121. [CrossRef] [PubMed]
25. Lee, Y.K.; Park, J.; Lu, W. Electronic and Bonding Properties of $LiMn_2O_4$ Spinel with Different Surface Orientations and Doping Elements and Their Effects on Manganese Dissolution. *J. Electrochem. Soc.* **2016**, *163*, A1359–A1368. [CrossRef]
26. Karim, A.; Fosse, S.; Persson, K.A. Surface Structure and Equilibrium Particle Shape of the $LiMn_2O_4$ Spinel from First-Principles Calculations. *Phys. Rev. B* **2013**, *87*, 075322. [CrossRef]
27. Ouyang, C.Y.; Zeng, X.M.; Sljivancanin, Z.; Baldereschi, A. Oxidation States of Mn Atoms at Clean and Al_2O_3-Covered $LiMn_2O_4$ (001) Surfaces. *J. Phys. Chem. C* **2010**, *114*, 4756–4759. [CrossRef]
28. Zhao, M.; Song, X.; Wang, F.; Dai, W.; Lu, X. Electrochemical Performance of Single Crystalline Spinel $LiMn_2O_4$ Nanowires in an Aqueous $LiNO_3$ Solution. *Electrochim. Acta* **2011**, *56*, 5673–5678. [CrossRef]
29. Hosono, E.; Kudo, T.; Honma, I.; Matsuda, H.; Zhou, H. Synthesis of Single Crystalline Spinel $LiMn_2O_4$ Nanowires for a Lithium Ion Battery with High Power Density. *Nano Lett.* **2009**, *9*, 1045–1051. [CrossRef]
30. Yang, Z.; Wang, Y.; Chen, X.; Wu, H.; Zhang, Y. Mg^{2+} and Ti^{4+} Co-Doped Spinel $LiMn_2O_4$ as Lithium-Ion Battery Cathode. *Chemistryselect* **2019**, *4*, 9583–9589. [CrossRef]
31. Xiong, L.; Xu, Y.; Zhang, C.; Zhang, Z.; Li, J. Electrochemical Properties of Tetravalent Ti-Doped Spinel $LiMn_2O_4$. *J. Solid State Electrochem.* **2011**, *15*, 1263–1269. [CrossRef]
32. Wei, Y.J.; Yan, L.Y.; Wang, C.Z.; Xu, X.G.; Wu, F.; Chen, G. Effects of Ni Doping on MnO_6 Octahedron in $LiMn_2O_4$. *J. Phys. Chem. B* **2004**, *108*, 18547–18551. [CrossRef]
33. Prabu, M.; Reddy, M.V.; Selvasekarapandian, S.; Rao, G.V.S.; Chowdari, B.V.R. (Li, Al)-Co-Doped Spinel, $Li(Li_{0.1}Al_{0.1}Mn_{1.8})O_4$ as High Performance Cathode for Lithium Ion Batteries. *Electrochim. Acta* **2013**, *88*, 745–755. [CrossRef]
34. Ram, P.; Singhal, R.; Choudhary, G.; Sharma, R.K. On the Key Role of Dy^{3+} in Spinel $LiMn_2O_4$ Cathodes for Li-Ion Rechargeable Batteries. *J. Electroanal. Chem.* **2017**, *802*, 94–99. [CrossRef]

35. Hashem, A.M.; Abdel-Ghany, A.E.; Abuzeid, H.M.; El-Tawil, R.S.; Indris, S.; Ehrenberg, H.; Mauger, A.; Julien, C.M. EDTA as Chelating Agent for Sol-Gel Synthesis of Spinel $LiMn_2O_4$ Cathode Material for Lithium Batteries. *J. Alloys.Compd.* **2018**, *737*, 758–766. [CrossRef]
36. Huang, S.; Wu, H.; Chen, P.; Guo, Y.; Nie, B.; Chen, B.; Liu, H.; Zhang, Y. Facile PH-Mediated Synthesis of Morphology-Tunable $MnCO_3$ and Their Transformation to Truncated Octahedral Spinel $LiMn_2O_4$ Cathode Materials for Superior Lithium Storage. *J. Mater. Chem. A* **2015**, *3*, 3633–3640. [CrossRef]
37. Liu, H.; Kloepsch, R.; Wang, J.; Winter, M.; Li, J. Truncated Octahedral $LiNi_{0.5}Mn_{1.5}O_4$ Cathode Material for Ultralong-Life Lithium-Ion Battery: Positive (100) Surfaces in High-Voltage Spinel System. *J. Power Sources* **2015**, *300*, 430–437. [CrossRef]
38. Liu, H.; Li, M.; Xiang, M.; Guo, J.; Bai, H.; Bai, W.; Liu, X. Effects of Crystal Structure and Plane Orientation on Lithium and Nickel Co-Doped Spinel Lithium Manganese Oxide for Long Cycle Life Lithium-Ion Batteries. *J. Colloid Interface Sci.* **2021**, *585*, 729–739. [CrossRef]
39. Dong, S.; Wang, X.; Shen, L.; Li, H.; Wang, J.; Nie, P.; Wang, J.; Zhang, X. Trivalent Ti Self-Doped $Li_4Ti_5O_{12}$: A High Performance Anode Material for Lithium-Ion Capacitors. *J. Electroanal. Chem.* **2015**, *757*, 1–7. [CrossRef]
40. Ben, L.; Yu, H.; Chen, B.; Chen, Y.; Gong, Y.; Yang, X.; Gu, L.; Huang, X. Unusual Spinel-to-Layered Transformation in $LiMn_2O_4$ Cathode Explained by Electrochemical and Thermal Stability Investigation. *ACS Appl. Mater. Interfaces* **2017**, *9*, 35463–35475. [CrossRef]
41. Tang, D.; Sun, Y.; Yang, Z.; Ben, L.; Gu, L.; Huang, X. Surface Structure Evolution of $LiMn_2O_4$ Cathode Material Upon Charge/Discharge. *Chem. Mater.* **2014**, *26*, 3535–3543. [CrossRef]
42. Biesinger, M.C.; Payne, B.P.; Grosvenor, A.P.; Lau, L.W.M.; Gerson, A.R.; Smart, R.S.C. Resolving Surface Chemical States in XPS Analysis of First Row Transition Metals, Oxides and Hydroxides: Cr, Mn, Fe, Co and Ni. *Appl. Surf. Sci.* **2011**, *257*, 2717–2730. [CrossRef]
43. Huang, R.; Ikuhara, Y.H.; Mizoguchi, T.; Findlay, S.D.; Kuwabara, A.; Fisher, C.A.J.; Moriwake, H.; Oki, H.; Hirayama, T.; Ikuhara, Y. Oxygen-Vacancy Ordering at Surfaces of Lithium Manganese(III,IV) Oxide Spinel Nanoparticles. *Angew. Chem. Int. Ed.* **2011**, *50*, 3053–3057. [CrossRef] [PubMed]
44. Pennycook, S.J.; Jesson, D.E. High-Resolution Z-Contrast Imaging of Crystals. *Ultramicroscopy* **1991**, *37*, 14–38. [CrossRef]
45. Chen, B.; Ben, L.; Yu, H.; Chen, Y.; Huang, X. Understanding Surface Structural Stabilization of the High-Temperature and High-Voltage Cycling Performance of Al^{3+}-Modified $LiMn_2O_4$ Cathode Material. *ACS Appl. Mater. Interfaces* **2018**, *10*, 550–559. [CrossRef] [PubMed]
46. Lin, M.; Ben, L.; Sun, Y.; Wang, H.; Yang, Z.; Gu, L.; Yu, X.; Yang, X.-Q.; Zhao, H.; Yu, R.; et al. Insight into the Atomic Structure of High-Voltage Spinel $LiNiO_3Mn_{1.5}O_4$ Cathode Material in the First Cycle. *Chem. Mater.* **2015**, *27*, 292–303. [CrossRef]
47. Xiao, B.W.; Liu, H.; Liu, J.; Sun, Q.; Wang, B.; Kaliyappan, K.; Zhao, Y.; Banis, M.N.; Liu, Y.; Li, R.; et al. Nanoscale Manipulation of Spinel Lithium Nickel Manganese Oxide Surface by Multisite Ti Occupation as High-Performance Cathode. *Adv. Mater.* **2017**, *29*, 1703754. [CrossRef]
48. Huang, M.R.; Lin, C.W.; Lu, H.Y. Crystallographic Facetting in Solid-State Reacted $LiMn_2O_4$ Spinel Powder. *Appl. Surf. Sci.* **2001**, *177*, 103–113. [CrossRef]
49. Zhang, H.; May, B.M.; Serrano-Sevillano, J.; Casas-Cabanas, M.; Cabana, J.; Wang, C.; Zhou, G. Facet-Dependent Rock-Salt Reconstruction on the Surface of Layered Oxide Cathodes. *Chem. Mater.* **2018**, *30*, 692–699. [CrossRef]
50. Gao, X.; Ikuhara, Y.H.; Fisher, C.A.J.; Huang, R.; Kuwabara, A.; Moriwake, H.; Kohama, K.; Ikuhara, Y. Oxygen Loss and Surface Degradation During Electrochemical Cycling of Lithium-Ion Battery Cathode Material $LiMn_2O_4$. *J. Mater. Chem. A* **2019**, *7*, 8845–8854. [CrossRef]
51. Gao, X.; Ikuhara, Y.H.; Fisher, C.A.J.; Moriwake, H.; Kuwabara, A.; Oki, H.; Kohama, K.; Yoshida, R.; Huang, R.; Ikuhara, Y. Structural Distortion and Compositional Gradients Adjacent to Epitaxial $LiMn_2O_4$ Thin Film Interfaces. *Adv. Mater. Interfaces* **2014**, *1*, 1400143. [CrossRef]
52. Maunders, C.; Martin, B.E.; Wei, P.; Petric, A.; Botton, G.A. Investigation of the Electronic Structure of the Cubic Spinel $Cu_{1.2}Mn_{1.8}O_4$ Using Electron Energy Loss Spectroscopy. *Solid State Ion* **2008**, *179*, 718–724. [CrossRef]
53. Schmid, H.K.; Mader, W. Oxidation States of Mn and Fe in Various Compound Oxide Systems. *Micron* **2006**, *37*, 426–432. [CrossRef] [PubMed]
54. Zhang, S.; Livi, K.J.T.; Gaillot, A.-C.; Stone, A.T.; Veblen, D.R. Determination of Manganese Valence States in (Mn^{3+}, Mn^{4+}) Minerals by Electron Energy-Loss Spectroscopy. *Am. Mineral.* **2010**, *95*, 1741–1746. [CrossRef]